



ELSEVIER

Contents lists available at ScienceDirect

## Journal of Magnetism and Magnetic Materials

journal homepage: [www.elsevier.com/locate/jmmm](http://www.elsevier.com/locate/jmmm)

## Research articles

## Predicting size-dependent heating efficiency of magnetic nanoparticles from experiment and stochastic Néel-Brown Langevin simulation

Ulrich M. Engelmann<sup>a,b,\*</sup>, Carolyn Shasha<sup>c</sup>, Eric Teeman<sup>b</sup>, Ioana Slabu<sup>a</sup>, Kannan M. Krishnan<sup>b,c,\*</sup><sup>a</sup> Applied Medical Engineering, Helmholtz Institute, Medical Faculty, RWTH Aachen University, 52074 Aachen, Germany<sup>b</sup> Department of Materials Science and Engineering, University of Washington, Seattle, WA 98195, USA<sup>c</sup> Department of Physics, University of Washington, Seattle, WA 98195, USA

## ARTICLE INFO

## Keywords:

Magnetic iron-oxide nanoparticles  
 Magnetic fluid hyperthermia  
 Particle core size  
 Monte Carlo simulation  
 Magnetic relaxation dynamics

## ABSTRACT

Magnetic nanoparticles (MNP) have been investigated for generating therapeutic heat when subjected to an alternating magnetic field (AMF) and applied for tumor-confined cancer therapy, so-called magnetic fluid hyperthermia (MFH). For application of MFH, a key requirement is the reduction of MNP dosing by maximizing the heat generation within medically safe limits of the applied AMF. Therefore, reliable and accurate predictions of particle heating are required for the advancement of therapy planning. In this study, we compare size-dependent particle heating data from calorimetric measurements to stochastic Néel-Brown Langevin equation Monte Carlo simulations, finding good agreement between them for various AMF amplitudes and frequencies. Within medical safety constraints of the AMF, our simulations predict maximum particle heating for magnetite particle core sizes above 25 nm with effective anisotropy constants  $K = 4000 \text{ J/m}^3$  at frequencies of  $\sim 100 \text{ kHz}$  and field amplitudes  $\sim 10 \text{ mT}/\mu_0$ . These simulations could help to predict the optimal combination of medically safe AMF parameters and MNP intrinsic properties, such as core size and effective anisotropy, to maximize heat generation and reduce MNP dosing in the application of MFH.

## 1. Introduction

Magnetic fluid hyperthermia (MFH) uses magnetic nanoparticles (MNP) as therapeutic heating agents to enable the release of heat, which is then dissipated into their immediate surroundings, e.g. a tumor, facilitating organ confined cancer treatment [1–3]. The MNP transform the energy of an externally applied alternating magnetic field (AMF) into heat via relaxation of their magnetic moments. MFH efficacy relies on MNP efficiency to generate heat, largely determined by the MNP concentration, magnetization and core size [4,5]. This heat generation offers great potential in minimally-invasive localized anticancer therapy, as demonstrated in clinical trials applying MFH successfully to prostate and brain tumors [6–8]. However, doubt has been cast recently on the effectiveness of hyperthermic therapy in general [9] and the MNP dosing necessary to induce therapeutically effective heating in particular [10]. Indeed, the iron concentration of iron-oxide MNP used in the above-mentioned clinical trials ( $\approx 112 \text{ mg(Fe)/mL}$ ) must be considered with care, as the long term toxicity of such high MNP dosing has not yet been evaluated [11]. Therefore, the maximization of particle heating at lower iron concentrations is a key

requirement for the advancement of MFH towards broader clinical application while ensuring patient safety [12].

The prediction of optimized particle heating has been widely addressed by theoretical descriptions and simulations, starting with the analytic particle heating model introduced by Rosensweig [13]. The model, named linear response theory (LRT), is highly popular due to its simplicity and applicability; however, it assumes a linear response of the MNP magnetization to the applied field, and is therefore limited to relatively small particle core sizes,  $d_c$ , and low field amplitudes,  $H_0$ , (e.g.  $H_0 \leq 11.4 \text{ mT}/\mu_0$  for  $d_c = 12 \text{ nm}$  and saturation magnetization  $M_S = 400 \text{ kA/m}$ ). Larger MNP ( $d_c \geq 20 \text{ nm}$ ) were described within the framework of the Stoner-Wohlfarth theory by Hergt et al. [14], which was adapted (with temperature-dependence) by Carrey et al. to the Stoner-Wohlfarth model based theory (SWMBT) and supported by numerical simulations [15]. These simulations used a simplified particle relaxation by assuming the so called 2-level-approximation, where particles can only have two effective states, separated by an energy barrier, while neglecting further excited states as well as Brownian rotation relaxation. Despite these simplifications, the work succeeded in demonstrating the incompatibility of LRT and SWMBT and highlighted

\* Corresponding authors at: Applied Medical Engineering (Helmholtz-Institute), Pauwelsstrasse 20, 52072 Aachen, Germany (U.M. Engelmann), Department of Materials Science and Engineering, 323 Roberts Hall, Box 352120, University of Washington, Seattle, WA, 98195, USA (K.M. Krishnan).

E-mail addresses: [engelmann@ame.rwth-aachen.de](mailto:engelmann@ame.rwth-aachen.de) (U.M. Engelmann), [kannanmk@uw.edu](mailto:kannanmk@uw.edu) (K.M. Krishnan).

<https://doi.org/10.1016/j.jmmm.2018.09.041>

Received 21 June 2018; Received in revised form 8 September 2018; Accepted 9 September 2018

Available online 03 October 2018

0304-8853/ © 2018 Elsevier B.V. All rights reserved.

the necessity of numerical simulations for a unified model of size-dependent particle heating. The 2-level-approximation was further expanded by Mamiya et al., adding Brownian rotation (via a torque) to the model [16,17], which enabled the prediction of heating for physically rotatable MNP. Moreover, dynamic hysteresis simulations solving the stochastic Landau-Lifshitz-Gilbert equation were presented to predict particle heating more accurately [18], even including magnetic dipole-dipole interactions [19]. However, the latter simulations still lack Brownian rotation to model the relaxation processes of particle heating realistically. Further, direct validation of the simulation results against experimental data is missing, even though it is essential for the reliable and meaningful prediction of particle heating to advance clinical translation of MFH.

Recently, the development of a novel imaging technique, called magnetic particle imaging (MPI), has required the development of MNP tracers to exploit their relaxation in comparatively low frequency fields ( $f_{\text{MPI}} \sim 25$  kHz versus  $f_{\text{MFH}} \sim 200$  kHz) for contrast enhancement [1,20]. It has been suggested, first theoretically [21] and then experimentally [22,23], that it may be possible to combine MPI diagnostic and MFH therapeutic application using the same MNP tracer. Although the present study focuses on MFH optimization, we will also briefly evaluate the MPI suitability of MNP systems for hybrid MFH-MPI application.

Here, we present MFH experimental heating results for four well-characterized magnetite particle systems of core sizes  $d_c = (22\text{--}28)$  nm, each with narrow size distribution, for various field frequencies and amplitudes. The experimental data is then matched by Monte Carlo (MC-) stochastic Néel-Brown Langevin equation simulations. This allows for the direct validation of our theoretical modelling and determination of suitable effective anisotropy constants. From this, we use the MC-simulations to predict the optimal combination of particle core size and AMF parameters maximizing the particle heating within medically tolerable constraints of the applied field.

## 2. Theory

### 2.1. Nonlinear particle relaxation dynamics

To study magnetic particle relaxation dynamics in an AMF with frequencies on the order of hundreds of kilohertz, as typically applied in MFH, we use dynamic Monte Carlo simulations in the framework of coupled stochastic differential Langevin equations. Details on these are found in [24]. Herein, the combined Néel-Brownian rotation relaxation dynamics for the general case of non-zero fields and non-equilibrium conditions are described. The internal magnetic particle moment,  $\mathbf{m}$ , rotates as expressed by the Landau-Lifshitz-Gilbert equation (LLG) [25], which is coupled with the equation of the generalized torque,  $\Theta$ , acting on the easy axis of the particles,  $\mathbf{n}$ , [26]:

$$\frac{d\mathbf{m}}{dt} = \frac{\mu_0\gamma}{1 + \alpha^2} \cdot (\mathbf{H} \times \mathbf{m} + \alpha \mathbf{m} \times (\mathbf{H} \times \mathbf{m})), \quad (1)$$

$$\frac{d\mathbf{n}}{dt} = \frac{\Theta}{6\eta V_H} \times \mathbf{n}, \quad (2)$$

with the permeability of free space  $\mu_0$ , electron gyromagnetic ratio,  $\gamma$ , the damping parameter,  $\alpha$ , the surrounding fluid viscosity,  $\eta$ , and the particle hydrodynamic volume,  $V_H = \pi/6 \cdot d_H^3$ , with the hydrodynamic particle size,  $d_H$ , which we differentiate from the magnetic core size, due to the addition of a non-magnetic coating. The effective field,  $\mathbf{H}$ , in Eq. (1) and the generalized torque,  $\Theta$ , in Eq. (2) can be derived from the particle energy:

$$U = -\mu_0\mu\mathbf{m} \cdot \mathbf{H}_{\text{app}} - KV_C(\mathbf{m} \cdot \mathbf{n})^2, \quad (3)$$

$\mu = |\mathbf{m}| = V_C M_S$  describes the magnitude of magnetic particle moment, with the particle core volume  $V_C = \pi/6 \cdot d_c^3$  and the saturation magnetization,  $M_S$ . The first term in Eq. (3) is associated with the

Zeeman term, including the interaction with the applied field,  $\mathbf{H}_{\text{app}}$ , while the second term describes the contributions of the effective anisotropy constant,  $K$ . We assume our particles to be uniformly dispersed, having high enough interparticle distance, so that magnetic dipole-dipole interactions are neglected here (see [Supplementary Material S1](#)). Using Eq. (3) and adding thermal fluctuations, the effective field and generalized torque can be derived as follows:

$$\mathbf{H} = -\frac{1}{\mu\mu_0} \cdot \frac{\partial U}{\partial \mathbf{m}} + \mathbf{H}_{\text{th}} = \mathbf{H}_{\text{app}} + \frac{2KV_C}{\mu\mu_0} \cdot (\mathbf{m} \cdot \mathbf{n})\mathbf{n} + \mathbf{H}_{\text{th}}, \quad (4)$$

$$\Theta = \frac{\partial U}{\partial \mathbf{n}} \times \mathbf{n} + \Theta_{\text{th}} = -2KV_C(\mathbf{m} \cdot \mathbf{n})(\mathbf{m} \times \mathbf{n}) + \Theta_{\text{th}}. \quad (5)$$

The thermally generated fields,  $\mathbf{H}_{\text{th}}$ , and torques,  $\Theta_{\text{th}}$ , are expressed as Gaussian-distributed processes with an approximately flat frequency distribution (white noise) with zero mean  $\langle \mathbf{H}_{\text{th}}^i(t) \rangle = 0$  and  $\langle \Theta_{\text{th}}^i(t) \rangle = 0$  and variances  $\langle \mathbf{H}_{\text{th}}^i(t) \mathbf{H}_{\text{th}}^j(t) \rangle = (2k_B T \cdot (1 + \alpha^2)) / (\gamma\mu\alpha) \cdot \delta_{ij} \delta(t-t')$  and  $\langle \Theta_{\text{th}}^i(t) \Theta_{\text{th}}^j(t) \rangle = 12k_B T \eta V_H \cdot \delta_{ij} \delta(t-t')$ . As described in our previous work [27], we use the Stratonovich-Heun scheme for numerical integration to account for the stochastic calculus terms in the white-noise limit [28].

### 2.2. Physics of particle heating

Particle relaxation in an AMF requires magnetic energy to align the individual magnetic particle moments parallel to the applied field against internal constraints caused by effective magnetic anisotropy. During field-driven relaxation processes, heat is generated equal to the magnetic energy consumed for this alignment in one cycle of the applied field (i.e. hysteresis loop,  $M(H)$ ) [16]. The hysteresis arises from the magnetization vector lagging behind the driving AMF vector. The heat is proportional to the area,  $A$ , of the hysteresis loop, expressed as [15]:

$$A = \int_{-H_0}^{H_0} \mu_0 M(H) dH, \quad (6)$$

with the magnetic permeability of free space,  $\mu_0$ , and the amplitude of the applied field,  $H_0$ . Commonly, the heating rate is expressed as the specific loss power (SLP), defined as the energy per unit time and per unit mass of nanoparticles. The theoretical SLP value follows with

$$\text{SLP} \left[ \frac{\text{kW}}{\text{g}} \right] = \mu_0 \cdot A \left[ \left( \frac{\text{kA}}{\text{m}} \right)^2 \right] \cdot \frac{f [\text{Hz}]}{\rho [\text{kg}/\text{m}^3]}, \quad (7)$$

where  $f$  denotes the applied field frequency and  $\rho$  the MNP material's mass density.

## 3. Material and methods

### 3.1. Particle synthesis and characterization

We have synthesized monodisperse iron-oxide (magnetite) MNP of four different core sizes via thermal decomposition of iron (III) oleate, coated with a co-polymer of poly(maleic anhydride-alt-1-octadecene) (PMAO) and poly(ethylene glycol) methyl ether amine (mPEG-NH<sub>2</sub>) as previously reported in [29,30]. The sample iron content ( $c$ ) was measured by inductively coupled plasma optical emission spectroscopy (ICP-OES) using an ICP-OES Optima 8300 device (PerkinElmer Inc., Waltham, MA, USA). Particle core size was measured by transmission electron microscopy (TEM) employing a FEI Tecnai TEM (ThermoFisher Scientific, Hillsboro, Oregon, USA) operated at 200 kV, equipped with a Gatan CCD camera. Particle core sizes ( $d_c$ ) were determined from a multitude of TEM images using the software ImageJ [31], and fitted with the log-normal distribution probability density function (PDF; see [Appendix A](#)). Furthermore, particle hydrodynamic size was measured by dynamic light scattering (DLS) with a Zetasizer Nano S (Malvern Instruments Ltd., Worcestershire, UK). MNP highly diluted in deionized

water (DI-H<sub>2</sub>O) were measured at 20 °C and analyzed with the Zetasizer software (Vers. 7.11, Malvern), yielding the mean hydrodynamic size ( $z_{\text{avg}}$ ) and its distribution width, called polydispersity index ( $PdI$ ). 100  $\mu\text{L}$  of liquid MNP samples were magnetically characterized with a vibrating sample magnetometer (VSM; Lakeshore Cryotronics Inc., Westerville, OH, USA) in the range of (–200...200) mT/ $\mu_0$  at ambient conditions. The resulting  $M(H)$  curves yielded the saturation magnetization ( $M_S$ ).

### 3.2. Calorimetric specific loss power measurements

Calorimetric particle heating measurements were carried out with a magneTherm 1.0 device (nanoTherics Ltd., Newcastle under Lyme, UK) consisting of a water-cooled copper coil (inner and outer diameter 44 mm and 54 mm, 17 turns) integrated in an AC-resonant circuit and a DC power generator. The field amplitude,  $H_0$ , and the frequency,  $f$ , were varied in the following way: At  $f = 176$  kHz, we varied  $H_0 = (6 \cdots 18)$  mT/ $\mu_0$  in increments of 3 mT/ $\mu_0$ , and for fixed  $H_0 = 6$  mT/ $\mu_0$ , we varied  $f = (176, 373, 744, 992)$  kHz. 0.25 mL samples were prepared in 0.5 mL PCR tubes, brought to an initial temperature of  $T = 25$  °C and exposed to the AMF for 180 s. Each sample was measured in triplicate, and the temperature was recorded using a fiber-optic thermometer Luxtron I652 (LumaSense Inc., Santa Barbara, CA, USA). Reference of pure DI-H<sub>2</sub>O samples were prepared and measured in the same way and served for background subtraction. The measured temperature-time curves were fitted with a linear function for the initial 60 s of applying the AMF, and from the slope,  $m$ , derived from the fitting, the SLP value was calculated according to [32]:

$$\text{SLP} = \frac{c}{\rho^*} \frac{dT}{dt} \Big|_{t \rightarrow 0}, \quad (8)$$

with the specific heat capacity of water,  $c$  ( $= 4.187$  J/g/°C), the MNP weight fraction,  $\rho^*$ , and  $dT/dt(t \rightarrow 0) = m$ , the initial temperature rise. The SLP value was averaged over the three triplicate measurements for each sample.

### 3.3. Stochastic Néel-Brown Langevin equation Monte Carlo simulation

Stochastic Néel-Brown Langevin equation Monte Carlo (MC-) simulations were performed within the framework described in the previous Section 2.1 at 300 K with uniaxial anisotropy. Generally, particle core size was varied from 10 nm to 30 nm in increments of 0.5 nm. Input parameters were fixed to a core size distribution width  $\sigma = 0.06$ , hydrodynamic size  $d_H = 75$  nm with distribution width  $\sigma_{d_H} = 0.12$ , and saturation magnetization  $M_S = 375$  kA/m. These parameters were chosen according to the average particle properties derived from particle characterization (cf. Table 1). The effective anisotropy constant and the damping parameter were varied from  $K = 4000$  J/m<sup>3</sup> to  $K = 11,000$  J/m<sup>3</sup> and  $\alpha = 0.5$  to  $\alpha = 1.0$ , respectively, in order to find the best match to the experimental data (see Section 4.2). 1,000 particles were simulated simultaneously with their magnetization averaged over 20 independent iterations. During simulation, the easy axis and magnetic moment orientation of each particle were initialized pointing in randomized directions. Subsequently, the particles magnetic moments were allowed to thermalize for one-fifth of the total time steps,

**Table 1**

Particle properties derived from characterization with ICP-OES, TEM, DLS and VSM measurements (see Section 3.1 for experimental details).  $c$  denotes the iron content,  $\mu$  and  $\sigma$  the log-normal distribution PDF fitting parameters,  $d_C$  the average core size,  $z_{\text{avg}}$  the hydrodynamic size,  $PdI$  the polydispersity index, and  $M_S$  the saturation magnetization.

Sample	$c$ [mg(Fe)/mL]	$\mu$ [nm]	$\sigma$	$d_C$ [nm]	$z_{\text{avg}}$ [nm]	$PdI$	$M_S$ [kA/m]
S1	1.498 ± 0.007	21.9	0.04	21.9 ± 0.9	94.1	0.130	346.3 ± 0.9
S2	1.315 ± 0.007	23.1	0.05	23.1 ± 1.2	55.4	0.127	376.4 ± 0.3
S3	1.513 ± 0.008	25.3	0.08	25.4 ± 2.0	48.6	0.104	389.1 ± 0.4
S4	1.499 ± 0.007	27.7	0.07	27.8 ± 1.9	97.0	0.121	362.8 ± 0.9

$N$ , used for the main simulation. Here, fixing  $N = 10,000$  was a good compromise between accuracy and computation time, resulting in simulation time steps on the order of 10–100 picoseconds. From the resulting magnetization vs. applied field curves (hysteresis loops),  $M(H)$ , the implicit area,  $A$ , was extracted and the SLP value calculated according to Eq. (7).

## 4. Results & discussion

### 4.1. Particle characterization

The results from particle characterization are summarized in Table 1.

The iron content of all samples, henceforth named S1 through S4, is within (1.31...1.51) mg(Fe)/mL (equivalent to approx. (0.13...0.15) m%). This allows for an estimation of the mean interparticle distance of approx. (240–300) nm for all samples, at which magnetic dipole-dipole interactions can be neglected (see Supplementary Material S1 for details) and corroborates our assumption to excluded magnetic dipole-dipole interactions from Eq. (3) in Section 2.1. Exemplary TEM images of the particles are shown in the Supplementary Material S2: The particle core sizes range from approx. 22 nm for S1 to 28 nm for S4 and the size distribution width is very narrow for each sample, confirming good monodispersity. Even though, hydrodynamic sizes varied with  $d_H \approx 95$  nm for S1 and S4, and  $d_H \approx 50$  nm for S2 and S3, the polydispersity index of  $PdI \approx 0.120$  further confirms monodispersity of all samples. The saturation magnetization  $M_S$  increases with particle core size as expected and consistent with literature [33] and confirms good magnetic properties with >75% bulk magnetite value (446 kA/m) for all samples as shown in Supplementary Material S3.

Please note that these MNP are well established as optimized MPI tracers [34–36], with applicability for in vivo imaging [37] and multicolor MPI [27] due to their precise size control. Generally, MNP with core sizes  $d_C = (25–28)$  nm are suited best as MPI tracers at 25 kHz excitation frequency (see Supplementary Material S4). We will discuss the suitability of these MNP for combined MFH-MPI application briefly in Section 4.3.

### 4.2. Size-dependent particle heating measurements and MC-Simulation

The results of size-dependent SLP measurements are shown for different frequencies and field amplitudes in Fig. 1a and b, respectively. Overall, the SLP values span a range of approx. (5...75) W/g(Fe<sub>3</sub>O<sub>4</sub>). As a general trend, we observe an increase in the SLP value with increasing field frequency or field amplitude, with highest SLP values achieved for  $f = 992$  kHz and  $H_0 = 18$  mT/ $\mu_0$ , respectively. SLP values also increase for larger particle core sizes; however, the relative difference between SLP values gets smaller for larger sizes (25.4 nm and 27.8 nm).

Such an increase in SLP values with increasing size was also reported for smaller sized magnetite MNP with  $d_C = (5–14)$  nm previously [38]. In contrast, Lima et al. have measured an increase in SLP value for magnetite MNP up to a core size approx. 18 nm, followed by a decrease in SLP value for particles with  $d_C = 23$  nm [39]. Additionally, Mehdaoui et al. found a similar trend for iron nanostructures (spherical and cubic MNP) in the size range from (5–28) nm, with a dramatic

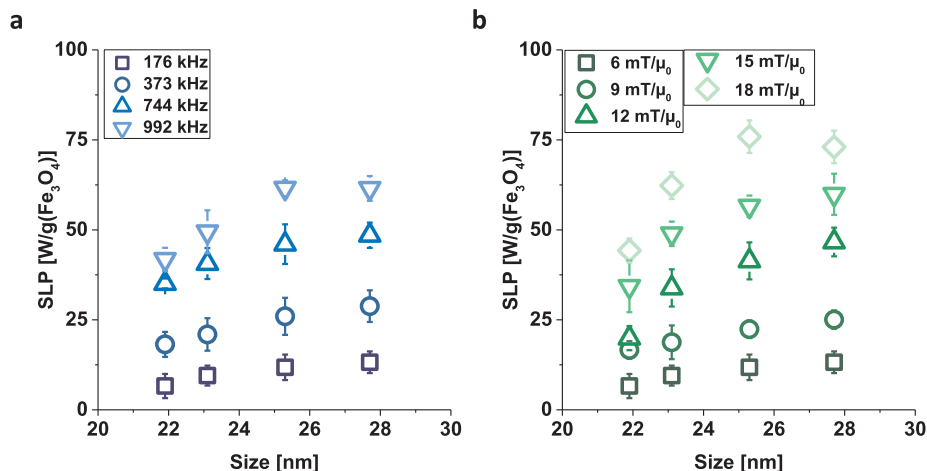


**Fig. 1.** Particle core size-dependent SLP values determined (a) for various frequencies at fixed  $H_0 = 6 \text{ mT}/\mu_0$  and (b) for various field amplitudes at fixed  $f = 176 \text{ kHz}$ . [2-column image].

decrease in SLP value for  $d_c = 28 \text{ nm}$  [40]. However, in the former case, the MNP concentration was 1 m%, strongly decreasing the mean interparticle distance to the regime where particle dipole-dipole interactions dominate, leading to an increase in the effective anisotropy constant,  $K$  [41]. In the latter case – using iron nanostructures – the effective anisotropy constant is much higher with  $K_{\text{Fe}} = 48,000 \text{ J/m}^3 > K_{\text{Fe}_3\text{O}_4} = 11,000 \text{ J/m}^3$  [42]. Here,  $K$  is possibly even further enhanced due to shape anisotropy contributions arising from the cubic shape of the nanostructures [43]. Indeed, increasing  $K$  leads to a global decrease in SLP values combined with a shift of the SLP maximum value towards smaller sizes, shown in the [Supplementary Material S5](#). A considerably higher  $K$  value could therefore account for the reported differences. This assumption is corroborated by the fact that the experimental heating data of our non-interacting MNP fits best to low  $K$  values, as we will demonstrate below.

We performed MC-simulations for various values of the effective anisotropy constant,  $K = (4000\text{--}11,000) \text{ J/m}^3$  with  $1000 \text{ J/m}^3$  increments, and damping parameter,  $\alpha = (0.5\text{--}1.0)$  with increments of 0.1 in the range of  $d_c = (10\text{--}30) \text{ nm}$  and compared the resulting curves to the experimental SLP values. Therefore, we normalized the experimental data to the highest SLP value (27.7 nm, 992 kHz for Fig. 1a and 25.4 nm,  $18 \text{ mT}/\mu_0$  for Fig. 1b). For the simulated curves, we normalized all curves to the highest value within the region ( $22 \leq d_c \leq 28$ ) nm for comparison to the experimental data, which was measured in the same size range. We calculated the  $\chi^2$ -parameter for each set of  $(K, \alpha)$  in the MC-simulation, and chose the best-fitting values as the ones minimizing the  $\chi^2$ -parameter. From this we obtain  $K = 4000 \text{ J/m}^3$  for effective anisotropy constant and a damping parameter  $\alpha = 0.7$ . The results comparing experimental SLP values (cf. Fig. 1) with the best-fitting MC-simulation data is summarized in Fig. 2.

In general, the  $\chi^2$ -test is used to determine whether experiment and theory agree statistically, showing best agreement for  $\chi^2/n_{\text{dof}} \cong 1$ , with the degrees of freedom,  $n_{\text{dof}}$  [44]. Here, however, we used the  $\chi^2$ -value to find the minimum difference between theory and experiment and therefore chose the set of  $(K, \alpha)$  minimizing the individual  $\chi^2$ -values. The individual fitting parameters of  $\chi^2 = (0.04\text{--}0.40)$  lead to good agreement of experimental and simulated data for the frequency-varied case (Fig. 2a). The agreement is equally good for the amplitude dependency with  $\chi^2 = (0.11\text{--}0.74)$ , except for the highest amplitude with  $\chi^2 = 3.28$  (Fig. 2b). This irregularity is mainly attributed to the experimental SLP value for  $18 \text{ mT}/\mu_0$  and  $d_c = 27.8 \text{ nm}$ , which does not follow the trend measured for all the other field amplitudes.

We believe that our MC-simulation protocol provides *quantitative* agreement with the experimental data for large MNP ( $d_c > 20 \text{ nm}$ ), unlike previous models and simulations mentioned in the introduction

[13–19,21,45]. For example, LRT only fits experimental data up to  $d_c = 13.5 \text{ nm}$  and  $H_0 = 6.8 \text{ mT}/\mu_0$  for cobalt ferrite MNP [45], while SWMBT fails to reproduce the size-dependent SLP-values measured for iron nanostructures for  $d_c > 20 \text{ nm}$  [40]. Optimum size predictions derived in [15] within the framework of SWMBT only fit experimental SLP values of magnetite MNP ( $d_c \approx 17 \text{ nm}$ ) when assuming extremely high effective anisotropy constants of  $K = (23,000\text{--}41,000) \text{ J/m}^3$  [46]. More advanced dynamic hysteresis simulations finally demonstrated the importance of tuning the effective anisotropy of MNP to optimize heating, but lack experimental validation [16,19]. Although the effective anisotropy constant,  $K = 4000 \text{ J/m}^3$ , used here is well below bulk value,  $K = 11,000 \text{ J/m}^3$ , for magnetite, it nevertheless fits well to earlier experimental value,  $K \approx 5000 \text{ J/m}^3$ , derived from magnetorheology, magnetic particle spectroscopy and AC-susceptibility measurements performed on our MNP with  $d_c \approx 20 \text{ nm}$  [47]. An even better agreement is observed for  $K = 4100 \text{ J/m}^3$ , derived very recently from fitting dynamical relaxation simulation data to experimental AC-susceptibility measurements of 21 nm core-sized MNP [48]. Therefore, and due to the very good quantitative agreement of experimental and simulated heating data achieved here, we confidently use the MC-simulations to predict optimized particle heating conditions under medical constraints in the next Section 4.3.

#### 4.3. Optimized particle heating under medical safety constraints

For a realistic prediction of MFH effectiveness in tumor therapy, the particle heating must be optimized with respect to the MNP system and the AMF parameters, which must at the same time remain within medically safe constraints. As the applied field can cause non-selective body heating and undesired nerve stimulation due to eddy currents, for practical biomedical applications the AMF must be limited to the “Brezovich-Criterion”, expressed in terms of the product of field amplitude and frequency, as  $H_0 \cdot f \leq Z_{\text{med}} = 615 \text{ kHz mT}/\mu_0$  [49]. In practice, higher tolerable AMF-limit were recorder, and clinical trials confirmed  $Z_{\text{med}}^{\text{body}} = 628 \text{ kHz mT}/\mu_0$  for AMF application at the lower body (rectum, prostate tumor) [6]. About three times higher limits of  $Z_{\text{med}}^{\text{head}} = 1758 \text{ kHz mT}/\mu_0$  were tolerated at the head (brain, glioblastoma multiforme tumor) [7]. Both limits agree well with  $Z_{\text{med}} \approx 1000 \text{ kHz mT}/\mu_0$  as suggested by the International Commission on Non-Ionizing Radiation Protection (ICNIRP) in their guidelines published for the public exposure limit to AMF [50]. In the following, we will consider MC-simulation results under the two constraints placed upon treatment of the body,  $Z_{\text{lim}}^{\text{body}} = H_0 \cdot f$ , and the head,  $Z_{\text{lim}}^{\text{head}} = H_0 \cdot f$ , varying  $f = (10\text{--}1000) \text{ kHz}$  and adjusting  $H_0$  in order not to exceed these limits. For practical reasons, we chose to vary frequency

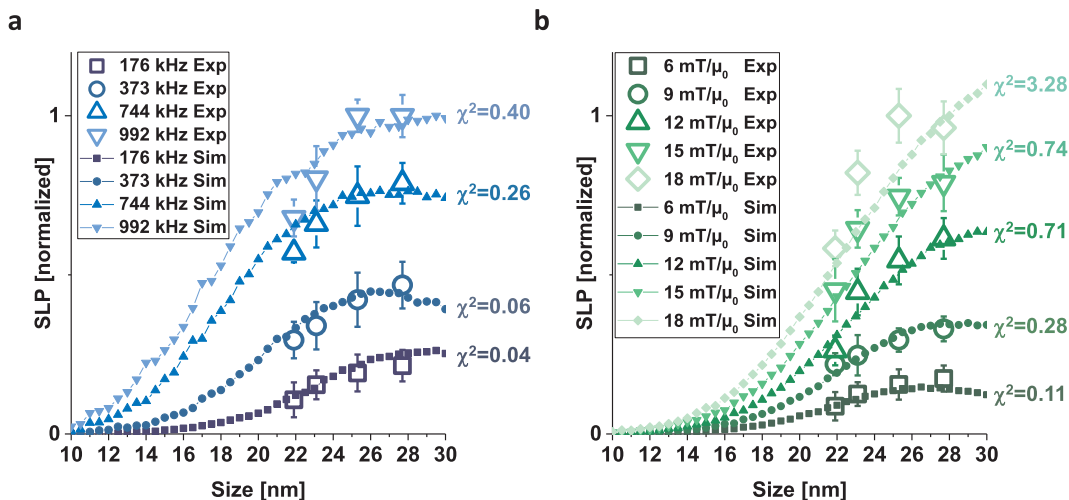


Fig. 2. Comparison of normalized size-dependent SLP values from experiment (open symbols) and dynamic Monte Carlo simulations (closed symbols) for various (a) frequencies at fixed  $H_0 = 6 \text{ mT}/\mu_0$ , and (b) field amplitudes at fixed  $f = 176 \text{ kHz}$ . Simulations were performed with an effective anisotropy  $K = 4000 \text{ J/m}^3$  and damping parameter  $\alpha = 0.7$ . The individual fitting parameters ( $\chi^2$ ) are shown next to each simulated curve. [2-column image].

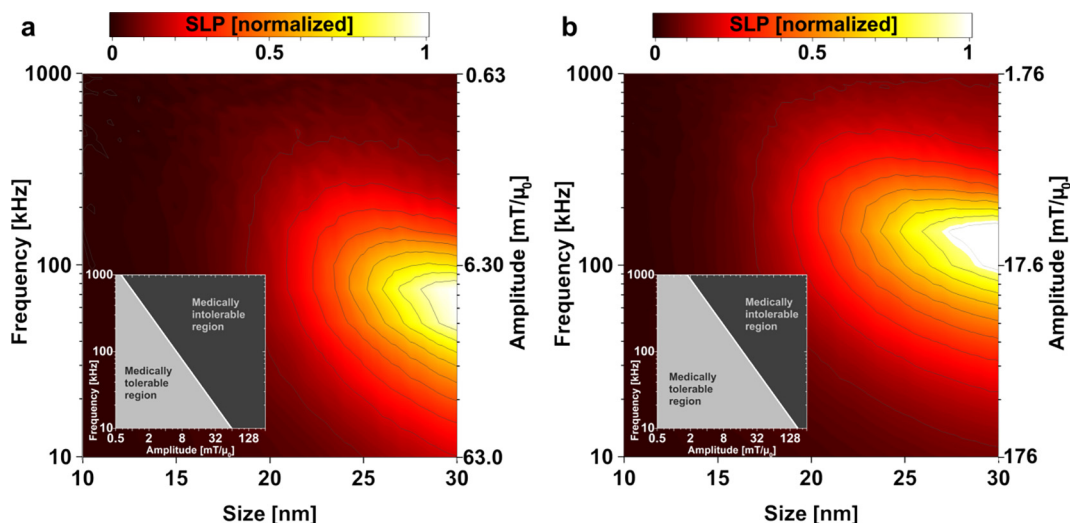


Fig. 3. Particle heating simulations depending on field parameters and particle core size under medical safety constraints: (a) for the body limit and (b) for the head limit. Inset graphs show the corresponding linear relationship of amplitude  $H_0$  vs. frequency  $f$  separating the medically tolerable from the intolerable region. [2-column image].

and adjust field amplitude accordingly, as in the hardware setting usually employing a resonant circuit consisting of coils and capacitors,  $f$  is fixed while  $H_0$  can be chosen accordingly. We used the damping parameter  $\alpha = 0.7$  and effective anisotropy constant  $K = 4000 \text{ J/m}^3$  and simulated for  $d_c = (10 \dots 30) \text{ nm}$ . The results are summarized in Fig. 3.

Generally, the highest heating under medical constraints occurs for the largest core sizes,  $d_c = (28 \dots 30) \text{ nm}$ , independent whether the body or head limit is applied. This is in line with the trend observed by Mamiya et al. for simulations of rotatable MNP within the 2-level approximation under similar medical constraints [51]. Since the product of  $H_0 f = Z_{\text{med}}$  is limited (cf. insets in Fig. 3), a distinct AMF setting generating highest particle heating can be clearly identified: For the body limit, we find highest SLP values at  $f_{\text{body}}^* \approx 75 \text{ kHz}$  ( $H_{0\text{body}}^* \approx 8.4 \text{ mT}/\mu_0$ ), while for the head limit, it shifts towards higher frequencies to  $f_{\text{head}}^* \approx 150 \text{ kHz}$  ( $H_{0\text{head}}^* \approx 11.7 \text{ mT}/\mu_0$ ). This means, if we assume similar  $K$ -values, that the AMF frequency of  $f = 100 \text{ kHz}$  used in the above-mentioned clinical trials [7] was optimal for reaching maximum SLP. Carrying the assumption further within our MC-simulation framework, these trials could have been even more effective by increasing the MNP core size from  $d_c = 15 \text{ nm}$  to e.g.  $d_c = 25 \text{ nm}$ , which

increases the predicted SLP-value from  $8.2 \text{ W/g}(\text{Fe}_3\text{O}_4)$  ( $d_c = 15 \text{ nm}$ ) to  $104.2 \text{ W/g}(\text{Fe}_3\text{O}_4)$  ( $d_c = 25 \text{ nm}$ ), translating in an amplification by a factor of  $\kappa \approx 12$  (cf. Fig. 3b). In other words, achieving the same heating while reducing MNP dosing by the same factor  $\kappa$  could have been possible, since the SLP-value is directly proportional to the MNP weight fraction (i.e. concentration; cf. Eq. (8)). This demonstrates the power and potential of accurate particle heating predictions for the advancement of treatment planning.

It is noteworthy, however, that the high MNP concentrations currently used in clinical MFH ( $c \approx 112 \text{ mg}(\text{Fe})/\text{mL}$ ; see Section 1) will inevitably induce MNP agglomeration resulting in collective MNP relaxation behavior [52]. The discussion, whether such collectively relaxing MNP agglomerates increases or decreases particle heating, is still ongoing and its effects are not fully understood at present [53,54]. Consequently, lowering MNP dosing in clinical application of MFH also helps to reduce uncertainty in predicting particle heating accurately.

From the intrinsic particle properties of core size and effective anisotropy, we can deduce that our particles with low effective anisotropy constant  $K \sim 4000 \text{ J/m}^3$  generate largest SLP values for large sizes  $d_c = (28 \dots 30) \text{ nm}$ . If, however, larger effective anisotropy constants are

employed, e.g. of the order of bulk magnetite value,  $K \sim 11,000 \text{ J/m}^3$ , the overall SLP value decreases and peaks at smaller sizes (cf. Supplementary Material S5). In fact, much higher than bulk  $K$ -values have been reported for small MNP ( $d_C \sim 10 \text{ nm}$ ), showing an increase in  $K$  for decreasing  $d_C$  arguably due to surface anisotropy arising from symmetry breaking at local surface defects [55,56]. Further development of the present MC-simulations for predicting optimized particle heating could therefore include a size-dependent effective anisotropy constant,  $K(d_C)$ : This would presumably increase the SLP value predictions for smaller sized particles,  $d_C < 20 \text{ nm}$ , which we did not consider for our study. Another future research opportunity could be the prediction of particle heating specifically for *in vivo* situations, where MNP are known to be inevitably internalized and immobilized inside cells [57]: As immobilization of MNP has been demonstrated to substantially decrease particle heating *in vivo* by inhibiting Brownian relaxation [48,58,59], additional simulations on predicting maximum SLP under restricted Brownian relaxation are envisioned to advance *in vivo* MFH therapy planning further.

Interestingly, considering the combined application of MPI and MFH, our largest sized particles (S4,  $d_C = 27.8 \text{ nm}$ ) present the optimal choice as imaging tracers and therapeutic heating agents at the same time. While MPI is generally assessed to be medically safe employing drive fields with frequencies up to  $f = 150 \text{ kHz}$  [60], we need to ensure medical safety while avoiding undesired heating of healthy tissue during imaging with such heating-optimized tracers. Therefore, we calculated the SLP value from MC-simulation for  $d_C = 27.8 \text{ nm}$  and typical MPI field amplitude  $H_0 = 20 \text{ mT}/\mu_0$  and frequency  $f = 25 \text{ kHz}$ . The resulting  $\text{SLP} \approx 10 \text{ W/g}(\text{Fe}_3\text{O}_4)$  would lead to a negligible temperature rise at typical MNP concentrations of  $c = 1 \text{ mg}(\text{Fe})/\text{mL}$  in a  $1 \text{ mL}$  volume [10]. Furthermore, we need to keep in mind that MNP used as MPI tracers will typically move within the blood or interstitial fluid, ideally only accumulating at the magnetically targeted tumor site. Consequently, sample S4 is well suited for a combined MPI-MFH biomedical application.

## 5. Conclusions

We investigated the size-dependent particle heating of

## Appendix A. Log-normal distribution probability density function

The log-normal distribution probability density function (PDF),  $g(d, \mu, \sigma)$ , is defined as

$$g(d, \mu, \sigma) = \frac{1}{\sqrt{2\pi} \cdot d \cdot \sigma} \cdot \exp\left(\frac{-\left(\ln\left(\frac{d}{\mu}\right)\right)^2}{2\sigma^2}\right) \quad (\text{A.1})$$

with the median,  $\mu$ , and the distribution width,  $\sigma$ , from which the mean and variance follow with  $d_C = \exp(\ln(\mu) + \sigma^2/2)$  and  $\sigma_d^2 = \exp(2\ln(\mu) + \sigma^2) \cdot (\exp(\sigma^2) - 1)$ , respectively.

## Appendix B. Supplementary data

Supplementary data to this article can be found online at <https://doi.org/10.1016/j.jmmm.2018.09.041>.

## References

- [1] K.M. Krishnan, Biomedical nanomagnetism: a spin through possibilities in imaging, diagnostics, and therapy: IEEE transactions on magnetism, IEEE Trans. Magn. 46 (2010) 2523–2558.
- [2] Q. Pankhurst, N. Thanh, S. Jones, J. Dobson, Progress in applications of magnetic nanoparticles in biomedicine, J. Phys. D Appl. Phys. 42 (2009) 224001.
- [3] Z. Hedayatnasab, F. Abnisa, W.M.A.W. Daud, Review on magnetic nanoparticles for magnetic nanofluid hyperthermia application, Mater. Des. 123 (2017) 174–196.
- [4] R. Hergt, S. Dutz, R. Müller, M. Zeisberger, Magnetic particle hyperthermia: nanoparticle magnetism and materials development for cancer therapy, J. Phys.: Condens. Matter 18 (2006) S2919.
- [5] C. Blanco-Andujar, F. Teran, D. Ortega, Current outlook and perspectives on nanoparticle-mediated magnetic hyperthermia, Iron Oxide Nanoparticles for Biomedical Applications, Elsevier, 2018, pp. 197–245.
- [6] M. Johannsen, U. Gneueckow, B. Thiesen, K. Taymoorian, C.H. Cho, N. Waldofner, R. Scholz, A. Jordan, S.A. Loening, P. Wust, Thermotherapy of prostate cancer using magnetic nanoparticles: feasibility, imaging, and three-dimensional temperature distribution, Eur. Urol. 52 (2007) 1653–1662.
- [7] K. Maier-Hauff, R. Rothe, R. Scholz, U. Gneueckow, P. Wust, B. Thiesen, A. Feussner, A. von Deimling, N. Waldofner, R. Felix, Intracranial thermotherapy using magnetic nanoparticles combined with external beam radiotherapy: results of a feasibility study on patients with glioblastoma multiforme, J. Neurooncol. 81 (2007) 53–60.
- [8] K. Mahmoude, A. Bouras, D. Bozec, R. Ivkov, C. Hadjipanayis, Magnetic hyperthermia therapy for the treatment of glioblastoma: a review of the therapy's history, efficacy, and application in humans, Int. J. Hyperther. (2018) 1–36.

monodisperse magnetic nanoparticles via experiment and MC-simulations of the nonlinear particle relaxation dynamics. Experimentally, we determined the SLP values for four samples with particle core sizes in the range of  $d_C = (22 \dots 28) \text{ nm}$  subjected to field amplitudes  $H_0 = (6 \dots 18) \text{ mT}/\mu_0$  and frequencies  $f = (176 \dots 992) \text{ kHz}$ . We observed a general increase in SLP values with increasing  $d_C$ ,  $H_0$  and  $f$ . Experimental data was matched by MC-simulations with quantitative agreement, providing validation of the MC-simulations. Moreover, MC-simulations revealed a strong dependence of SLP values on the effective anisotropy constant, of which  $K = 4000 \text{ J/m}^3$  fit our data best, in good agreement with previously measured  $K$ -values. On the basis of the experimentally verified MC-simulation parameters and under limitation of the AMF applied to the body or head to medically tolerable values, we predicted maximum SLP values in the frequency regime  $f = (75 \dots 150) \text{ kHz}$ , while assuming simultaneous maximization of  $H_0$  within the medical limit. Provided that the effective anisotropy is well known, our simulations provide a versatile and powerful tool for predicting the ideal particle and applied field parameters for optimal particle heating. From these predictions, particles showing optimal heating under consideration of the medically safety constraints could be produced to reduce the MNP dosing used in clinical application of MFH. Such optimization could highly improve patient safety, provided appropriate MNP dosing can be delivered *in vivo* to the targeted site.

## Acknowledgements

U.E. was supported by the German Federal Fellowship Cusanuswerk e.V.. C.S. was supported by a National Science Foundation Graduate Research Fellowship under Grant DGE-1256082. Simulations were performed with computing resources granted by RWTH Aachen University, Germany under project rwth0301.

## Declaration of interest

None.

- [9] S. Roussakow, The history of hyperthermia rise and decline, *Conference Papers in Science*, Hindawi, 2013.
- [10] P. Southern, Q.A. Pankhurst, Commentary on the clinical and preclinical dosage limits of interstitially administered magnetic fluids for therapeutic hyperthermia based on current practice and efficacy models, *Int. J. Hypertherm.* (2017) 1–16.
- [11] B. Schiller, P. Bhat, A. Sharma, Safety and effectiveness of ferumoxytol in hemodialysis patients at 3 dialysis chains in the United States over a 12-month period, *Clin. Ther.* 36 (2014) 70–83.
- [12] S.V. Spirou, S.A. Costa Lima, P. Bouziotis, S. Vranješ-Djurić, E.K. Efthimiadou, A. Laurenzana, A.I. Barbosa, I. Garcia-Alonso, C. Jones, D. Jankovic, Recommendations for in vitro and in vivo testing of magnetic nanoparticle hyperthermia combined with radiation therapy, *Nanomaterials* 8 (2018) 306.
- [13] R.E. Rosensweig, Heating magnetic fluid with alternating magnetic field, *J. Magn. Magn. Mater.* 252 (2002) 370–374.
- [14] R. Hergt, S. Dutz, M. Roder, Effects of size distribution on hysteresis losses of magnetic nanoparticles for hyperthermia, *J. Phys.-Condens. Matter* 20 (2008).
- [15] J. Carrey, B. Mehdaoui, M. Respaud, Simple models for dynamic hysteresis loop calculations of magnetic single-domain nanoparticles: application to magnetic hyperthermia optimization, *J. Appl. Phys.* 109 (2011) 083921.
- [16] H. Mamiya, B. Jeyadevan, Hyperthermic effects of dissipative structures of magnetic nanoparticles in large alternating magnetic fields, *Sci. Rep.* 1 (2011).
- [17] H. Mamiya, B. Jeyadevan, Formation of nonequilibrium magnetic nanoparticle structures in a large alternating magnetic field and their influence on magnetic hyperthermia treatment, *IEEE Trans. Magn.* 48 (2012) 3258–3261.
- [18] E.L. Verde, G.T. Landi, M.S. Carrião, A.L. Drummond, J.A. Gomes, E.D. Vieira, M.H. Sousa, A.F. Bakuzis, Field dependent transition to the non-linear regime in magnetic hyperthermia experiments: comparison between maghemite, copper, zinc, nickel and cobalt ferrite nanoparticles of similar sizes, *AIP Adv.* 2 (2012) 032120.
- [19] S. Ruta, R. Chantrell, O. Hovorka, Unified model of hyperthermia via hysteresis heating in systems of interacting magnetic nanoparticles, *Sci. Rep.* 5 (2015) 9090.
- [20] P.W. Goodwill, E.U. Saritas, L.R. Croft, T.N. Kim, K.M. Krishnan, D.V. Schaffer, S.M. Conolly, X-space MPI: magnetic nanoparticles for safe medical imaging, *Adv. Mater.* 24 (2012) 3870–3877.
- [21] R. Dhavalikar, C. Rinaldi, Theoretical predictions for spatially-focused heating of magnetic nanoparticles guided by magnetic particle imaging field gradients, *J. Magn. Magn. Mater.* 419 (2016) 267–273.
- [22] D. Hensley, Z.W. Tay, R. Dhavalikar, B. Zheng, P. Goodwill, C. Rinaldi, S. Conolly, Combining magnetic particle imaging and magnetic fluid hyperthermia in a theranostic platform, *Phys. Med. Biol.* 62 (2017) 3483–3500.
- [23] Z.W. Tay, P. Chandrasekharan, A. Chiu-Lam, D.W. Hensley, R. Dhavalikar, X.Y. Zhou, E.Y. Yu, P.W. Goodwill, B. Zheng, C. Rinaldi, Magnetic particle imaging-guided heating in vivo using gradient fields for arbitrary localization of magnetic hyperthermia therapy, *ACS Nano* 12 (2018) 3699–3713.
- [24] W. Coffey, P. Cregg, Y. Kalmykov, On the theory of Debye and Néel relaxation of single domain ferromagnetic particles, *Adv. Chem. Phys.* 83 (2007) 263–464.
- [25] T.L. Gilbert, A phenomenological theory of damping in ferromagnetic materials, *IEEE T Magn* 40 (2004) 3443–3449.
- [26] N. Usov, B.Y. Liubimov, Dynamics of magnetic nanoparticle in a viscous liquid: application to magnetic nanoparticle hyperthermia, *J. Appl. Phys.* 112 (2012) 023901.
- [27] C. Shasha, E. Teeman, K.M. Krishnan, Harmonic simulation study of simultaneous nanoparticle size and viscosity differentiation, *IEEE Magn. Lett.* 8 (2017) 1–5.
- [28] D.B. Reeves, J.B. Weaver, Combined Néel and Brown rotational Langevin dynamics in magnetic particle imaging, sensing, and therapy, *Appl. Phys. Lett.* 107 (2015) 223106.
- [29] S.J. Kemp, R.M. Ferguson, A.P. Khandhar, K.M. Krishnan, Monodisperse magnetite nanoparticles with nearly ideal saturation magnetization, *RSC Adv.* 6 (2016) 77452–77464.
- [30] R. Hufschmid, H. Arami, R.M. Ferguson, M. Gonzales, E. Teeman, L.N. Brush, N.D. Browning, K.M. Krishnan, Synthesis of phase-pure and monodisperse iron oxide nanoparticles by thermal decomposition, *Nanoscale* 7 (2015) 11142–11154.
- [31] C.A. Schneider, W.S. Rasband, K.W. Eliceiri, NIH Image to ImageJ: 25 years of image analysis, *Nat. Methods* 9 (2012) 671.
- [32] R.R. Wildeboer, P. Southern, Q.A. Pankhurst, On the reliable measurement of specific absorption rates and intrinsic loss parameters in magnetic hyperthermia materials, *J. Phys. D-Appl. Phys.* 47 (2014).
- [33] P. Hu, L. Kang, T. Chang, F. Yang, H. Wang, Y. Zhang, J. Yang, K.-S. Wang, J. Du, Z. Yang, High saturation magnetization Fe<sub>3</sub>O<sub>4</sub> nanoparticles prepared by one-step reduction method in autoclave, *J. Alloys Compd.* 728 (2017) 88–92.
- [34] R.M. Ferguson, A.P. Khandhar, C. Jonasson, J. Blomgren, C. Johansson, K.M. Krishnan, Size-dependent relaxation properties of monodisperse magnetite nanoparticles measured over seven decades of frequency by ac susceptometry, *IEEE Trans. Magn.* 49 (2013) 3441–3444.
- [35] R.M. Ferguson, A.P. Khandhar, S.J. Kemp, H. Arami, E.U. Saritas, L.R. Croft, J. Konkole, P.W. Goodwill, A. Halkola, J. Rahmer, Magnetic particle imaging with tailored iron oxide nanoparticle tracers, *IEEE Trans. Med. Imaging* 34 (2015) 1077–1084.
- [36] A.P. Khandhar, R.M. Ferguson, H. Arami, K.M. Krishnan, Monodisperse magnetite nanoparticle tracers for in vivo magnetic particle imaging, *Biomaterials* 34 (2013) 3837–3845.
- [37] H. Arami, A.P. Khandhar, A. Tomitaka, E. Yu, P.W. Goodwill, S.M. Conolly, K.M. Krishnan, In vivo multimodal magnetic particle imaging (MPI) with tailored magneto/optical contrast agents, *Biomaterials* 52 (2015) 251–261.
- [38] M. Gonzales-Weimuller, M. Zeisberger, K.M. Krishnan, Size-dependent heating rates of iron oxide nanoparticles for magnetic fluid hyperthermia, *J. Magn. Magn. Mater.* 321 (2009) 1947–1950.
- [39] E. Lima, E. De Biasi, M.V. Mansilla, M.E. Saleta, M. Granada, H.E. Troiani, F.B. Effenberger, L.M. Rossi, H.R. Rechenberg, R.D. Zysler, Heat generation in agglomerated ferrite nanoparticles in an alternating magnetic field, *J. Phys. D Appl. Phys.* 46 (2013) 045002.
- [40] B. Mehdaoui, A. Meffre, J. Carrey, S. Lachaize, L.-M. Lacroix, M. Gougeon, B. Chaudret, M. Respaud, Optimal size of nanoparticles for magnetic hyperthermia: a combined theoretical and experimental study, *Adv. Funct. Mater.* 21 (2011) 4573–4581.
- [41] L.C. Branquinho, M.S. Carrião, A.S. Costa, N. Zufelato, M.H. Sousa, R. Miotto, R. Ivkov, A.F. Bakuzis, Effect of magnetic dipolar interactions on nanoparticle heating efficiency: implications for cancer hyperthermia, *Sci. Rep.-UK* 3 (2013).
- [42] L. Bickford, J. Brownlow, R. Penoyer, Magnetocrystalline anisotropy in cobalt-substituted magnetite single crystals, *Proc. IEE-Part B: Radio Electronic Eng.* 104 (1957) 238–244.
- [43] K.M. Krishnan, *Fundamentals and Applications of Magnetic Materials*, Oxford University Press, 2016.
- [44] R.J. Barlow, *Statistics: A Guide to the Use of Statistical Methods in the Physical Sciences*, John Wiley & Sons, 1989.
- [45] E.L. Verde, G.T. Landi, J.D.A. Gomes, M.H. Sousa, A.F. Bakuzis, Magnetic hyperthermia investigation of cobalt ferrite nanoparticles: comparison between experiment, linear response theory, and dynamic hysteresis simulations, *J. Appl. Phys.* 111 (2012) 123902.
- [46] A.P. Khandhar, R.M. Ferguson, J.A. Simon, K.M. Krishnan, Tailored magnetic nanoparticles for optimizing magnetic fluid hyperthermia, *J. Biomed. Mater. Res. Part A* 100A (2012) 728–737.
- [47] F. Ludwig, H. Remmer, C. Kuhlmann, T. Wawrzik, H. Arami, R.M. Ferguson, K.M. Krishnan, Self-consistent magnetic properties of magnetite tracers optimized for magnetic particle imaging measured by ac susceptometry, magnetorelaxometry and magnetic particle spectroscopy, *J. Magn. Magn. Mater.* 360 (2014) 169–173.
- [48] D. Cabrera, A. Coene, J. Leliaert, E.J. Artes-Ibanez, L. Dupre, N.D. Telling, F.J. Teran, Dynamical magnetic response of iron oxide nanoparticles inside live cells, *ACS Nano* 12 (2018) 2741–2752.
- [49] W.J. Atkinson, I.A. Brezovich, D.P. Chakraborty, Usable frequencies in hyperthermia with thermal seeds, *IEEE Trans. Biomed. Eng.* 31 (1984) 70–75.
- [50] I.C.o.N.-I.R. Protection, Guidelines for limiting exposure to time-varying electric and magnetic fields (1 Hz to 100 kHz), *Health Phys.* 99 (2010) 818–836.
- [51] H. Mamiya, B. Jeyadevan, Optimal design of nanomagnets for targeted hyperthermia, *J. Magn. Magn. Mater.* 323 (2011) 1417–1422.
- [52] C. Dennis, A. Jackson, J. Borchers, R. Ivkov, A. Foreman, J. Lau, E. Goernitz, C. Gruettner, The influence of collective behavior on the magnetic and heating properties of iron oxide nanoparticles, *J. Appl. Phys.* 103 (2008) 07A319.
- [53] F. Spizzo, P. Sgarbossa, E. Sieni, A. Semenzato, F. Dughiero, M. Forzan, R. Bertani, L. Del Bianco, Synthesis of ferrofluids made of iron oxide nanoflowers: interplay between carrier fluid and magnetic properties, *Nanomaterials* 7 (2017) 373.
- [54] U. Engelmann, E.M. Buhl, M. Baumann, T. Schmitz-Rode, I. Slabu, Agglomeration of magnetic nanoparticles and its effects on magnetic hyperthermia, *Curr. Directions Biomed. Eng.* 3 (2017) 457–460.
- [55] K. Gilmore, Y.U. Idzerda, M.T. Klem, M. Allen, T. Douglas, M. Young, Surface contribution to the anisotropy energy of spherical magnetite particles, *J. Appl. Phys.* 97 (2005) 10B301.
- [56] G. Salazar-Alvarez, J. Qin, V. Sepelak, I. Bergmann, M. Vasilakaki, K. Trohidou, J. Ardisson, W. Macedo, M. Mikhaylova, M. Muhammed, Cubic versus spherical magnetic nanoparticles: the role of surface anisotropy, *J. Am. Chem. Soc.* 130 (2008) 13234–13239.
- [57] C. Wilhelm, F. Gazeau, Universal cell labelling with anionic magnetic nanoparticles, *Biomaterials* 29 (2008) 3161–3174.
- [58] R. Di Corato, A. Espinosa, L. Lartigue, M. Tharaud, S. Chat, T. Pellegrino, C. Menager, F. Gazeau, C. Wilhelm, Magnetic hyperthermia efficiency in the cellular environment for different nanoparticle designs, *Biomaterials* 35 (2014) 6400–6411.
- [59] U. Engelmann, A. Roeth, D. Eberbeck, E.M. Buhl, U. Neumann, T. Schmitz-Rode, I. Slabu, Combining bulk temperature and nanoheating enables advanced magnetic fluid hyperthermia efficacy on pancreatic tumor cells, *Sci. Rep.-UK* 8 (2018).
- [60] I. Schmale, B. Gleich, J. Rahmer, C. Bontus, J. Schmidt, J. Borgert, MPI safety in the view of MRI safety standards, *IEEE Trans. Magn.* 51 (2015) 1–4.